Journal of Applied Fluid Mechanics, Vol. 16, No. 8, pp. 1640-1653, 2023.
Available online at www.jafmonline.net, ISSN 1735-3572, EISSN 1735-3645.
https://doi.org/10.47176/jafm.16.08.1696

Study on the Erosion Characteristics of Non-spherical Particles in Liquid-solid Two-phase Flow

H. Z. Jin[1], Z. Y. Liao[1], J. F. Zhou[2], X. F. Liu[1], H. C. Yao[1] and C. Wang [1†]

[1]*Institute of Flow-Induced Corrosion, Zhejiang Sci-Tech University, Hangzhou, Zhejiang, 310018, China*
[2]*Hangzhou Special Equipment Inspection and Research Institute, Hangzhou 310051, China*

†*Corresponding Author Email:* wangchao@zstu.edu.cn

ABSTRACT

Elbow erosion, defined as wall thinning due to the continuous interactions between solid particles and surface, is a common phenomenon in catalyst addition/withdrawal pipeline systems used in residual oil hydrogenation units. This form of erosion can seriously affect the reliable pipeline operation. The present paper describes the construction of realistic cylindrical catalyst particles using the multi-sphere clump method and computational fluid dynamics/discrete element model simulations to study the erosion of pipe walls under different inlet velocities and particle aspect ratios. An optical shooting experiment is carried out to ensure the accuracy of the calculation method, and the model performance is compared using several existing drag models. The results show that the drag model of Haider & Levenspiel is more accurate than the others in revealing the actual cylindrical particle flow. A higher inlet velocity is observed to increase the kinetic energy of the particles and affect their spatial distribution. Specifically, when the Stokes number is greater than 113.7, the position of the maximum erosion rate shifts from the elbow's outer wall to the inner wall. Cumulative contact energy is introduced to quantify two different types of particle-wall contacts. With a growing particle aspect ratio, the proportion of tangential energy gradually increases, which indicates that sliding is the main contact mode. The results presented in this paper provide a reference for engineering erosion calculations.

Article History

Received December 1, 2022
Revised March 12, 2023
Accepted March 31, 2023
Available online May 31, 2023

Keywords:

Elbow
CFD-DEM
Drag model
Stokes number
Slide

1. INTRODUCTION

Boiling bed residue units that enable online catalyst addition and withdrawal are widely used in residual oil hydrogenation. The process of catalyst transportation is a typical complex liquid–solid flow, and the pipelines used to convey the catalysts often experience erosion problems.

Erosion is the phenomenon of material removal from the pipe walls through particle–surface interactions Many investigations have attempted to provide a better understanding of the erosion process. For example, Finnie et al. (1960, 1979) researched erosion mechanisms for brittle and ductile materials and proposed a widely accepted micro-cutting theory. Bitter (1962) believed that the combined effect of micro-cutting and impact deformation caused erosion. Based on the work of Finnie and Bitter, Deng et al. (2004) established a quantitative model that explains the effect of the particle spin direction on erosion by testing the velocity of the contact point between the spin particles and the target surface. Under specific experimental conditions, Archard (1953), Oka (2005), and the Erosion/Corrosion Research Center (Ahlert, 1994) established several classic erosion models. Recently, high-speed photography has been used to record the particle–wall collision behavior. Jing et al. (2018) investigated the particle velocity fields in gas–liquid–solid flows using image processing techniques, and found that the average deviation between the measured and numerical velocity was 6.1%. Wang et al. (2020) measured the collision velocities of non-spherical glass particles, and reported that the particle sphericity exhibited a strong relationship with the restitution coefficient *e*. As the impact angle approached 90°, the value of *e* reached0.6 for spherical particles and just 0.2–0.3 for non-spherical particles.

Full quantitative information about the flow field and particle motion parameters cannot be readily obtained by experiments. Numerical models have therefore been extensively developed (Ali, 2022; Sajjad et al., 2022). To date, most elbow erosion

Nomenclature

a_f	void ratio	Ar	aspect ratio
C_D	drag coefficient	D	inner diameter
e	restitution coefficient	E_n	normal cumulative contact energy
E_t	tangential cumulative contact energy	F_c	contact force
F_{drag}	drag force	F_p	pressure gradient force
F_{RL}	Magnus lift force	F_{vm}	added mass force
P	fluid pressure	R	radius of curvature
Re_p	Reynolds number of particle	St	Stokes number
u	fluid velocity	V_p	particle velocity
$y+$	dimensionless wall distance	μ_{eff}	fluid effective viscosity
φ_s	particle shape factor		

numerical studies have been performed using computational fluid dynamics (CFD) with a discrete particle model (DPM), enabling a series of significant achievements (Singh et al., 2019; Adedeji et al., 2020; Wang et al., 2021; Zolfagharnasab et al., 2021). As a common model for predicting the behavior of solid particles in the elbow region of a pipeline, DPM does not consider the particle volume. The discrete element model (DEM) allows the accurate capture of particle-scale information, including particle–particle interactions and particle shapes, which cannot be ignored in the actual transport process with large particles. CFD-DEM modeling is effective in particle–fluid systems (Yu & Xu, 2003; Tsuji et al., 2008; Gao et al., 2022; Ou et al., 2022), and has frequently been adopted for elbow erosion studies (Wang et al., 2017; Liu et al., 2022). Chen et al. (2015) compared the erosion that occurred at bends of different angles (45°, 60°, and 90°), and observed the maximum erosion rate in 90° elbows with the maximum erosion position for all elbows at or near the exit. Chen et al. (2022) studied the erosion rate of an elbow in the pneumatic transportation of stiff shotcrete. Based on the CFD-DEM method, the air velocity was found to have significant effects on particle velocity, but no effects on the particles' spatial positions. Spheres are commonly used to represent particles in DEM studies, making it easier to detect contact and calculate the associated forces. The flow characteristics of non-spherical particles also need to be investigated because of their applicability in real industrial processes. Non-spherical particles can be represented by either single or composite particles. In a single-particle method, the shape of the particle is described by a continuous function representation or a discrete function representation (Lu et al., 2012). The contact judgment of multi-sphere clumps is performed with the aid of internal child particles. Due to their flexibility, multi-sphere clumps have been extensively applied to construct non-spherical particles. Zhou et al. (2017) modeled real coal particles using the multi-sphere clump method, and reported that the mean erosion rate generally varies with the particle sphericity according to an inclined "S" pattern. Zeng et al. (2018) modeled four common polyhedral particles, and found that when the sphericity s<0.77, the main influencing factors for the erosion rate are the impact velocity and impact angle; when s>0.77, the main influencing factors are the impact concentration.

Erosion under liquid–solid flow is a complex physical problem consisting of two processes: particle–fluid flow and particle–wall contact. For the former, the drag force imposed by the fluid is a major cause of modification to the particle motion state. However, previous research on the erosion caused by non-spherical particles demonstrates the effectiveness of predictions given by maximum wear depth measurements, and there has been no experimental validation of drag models in multiphase flows. The motion of cylindrical catalyst particles would vary according to their geometric shape, thus affecting the flow erosion characteristics. The particle–wall contact is directly linked to particle collision dynamics. Previous studies lack detailed statistical information on the collision process and do not provide quantitative assessments for judging the particle–wall contact pattern.

In this paper, a two-way coupled Eulerian–Lagrangian approach is employed to investigate the erosion caused by a liquid–solid two-phase flow in the elbow sections of a pipeline. To verify the most appropriate drag model for cylindrical particles, a liquid–solid two-phase circulation experiment is performed and the particles' spatial distribution is captured by a high-speed camera. The effects of the inlet velocity and particle aspect ratio on erosion is then assessed. The analysis focuses on the effect of the particle Stokes number on the maximum erosion position and cumulative contact energy of the pipe walls.

2. METHODOLOGIES

The fluid is treated as a continuous phase and solved by the Navier–Stokes equations, while the particle motion is solved by tracking in a Lagrangian model.

2.1 Governing Equations for Fluid

The Reynolds-Averaged Navier-Stokes (RANS) equations are employed for the flow field modeling. The continuity and momentum conservation equations of the continuous phase are given as follows:

$$\frac{\partial}{\partial t}(\alpha_f \rho_f) + \frac{\partial}{\partial x_j}(\alpha_f \rho_f u_j) = 0 \tag{1}$$

$$\frac{\partial}{\partial t}(\alpha_f \rho_f u_i) + \frac{\partial}{\partial x_j}(\alpha_f \rho_f u_i u_j) = -\frac{\partial p}{\partial x_i} + \frac{\partial}{\partial x_j}\left[\alpha_f \mu_{eff}\left(\frac{\partial u_i}{\partial x_j} + \frac{\partial u_j}{\partial x_i}\right)\right] + \alpha_f \rho_f \boldsymbol{g} + \boldsymbol{F}_s \tag{2}$$

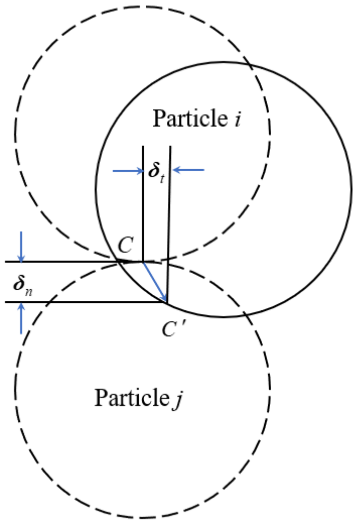

Fig. 1. Soft sphere model.

where ρ_f is the fluid density, u is the fluid velocity, p is the pressure of the fluid, μ_{eff} is the effective viscosity, $\boldsymbol{g}$ is gravitational acceleration, α_f is the void ratio, and $\boldsymbol{F}_s$ is the interaction term between particles and fluid. In addition, the realizable k-ε model is selected to resolve the turbulent flow, and the standard wall functions are applied to model the flow in the near-wall region.

2.2 Governing Equations for Particles

The particle motion includes both translation and rotation, which can be described by Newton's second law as

$$m\frac{d\boldsymbol{v}}{dt} = m\boldsymbol{g} + \sum \boldsymbol{F}_{drag} + \boldsymbol{F}_{RL} + \boldsymbol{F}_{vm} + \boldsymbol{F}_p + \boldsymbol{F}_c \tag{3}$$

$$\mathrm{I}\frac{d\boldsymbol{\omega}}{dt} = \sum \boldsymbol{T}_c + \boldsymbol{T}_f \tag{4}$$

where $\boldsymbol{v}$ and $\boldsymbol{\omega}$ are the translation and rotation velocities, respectively, $\boldsymbol{F}_{drag}$, $\boldsymbol{F}_{RL}$, $\boldsymbol{F}_p$, $\boldsymbol{F}_{vm}$, and $\boldsymbol{F}_C$ represent the drag force, Magnus lift force, pressure gradient force, added mass force, and particle–particle and particle–wall contact forces, respectively, and $\boldsymbol{T}_c$, $\boldsymbol{T}_f$ are the contact torque and the torque caused by fluid, respectively.

As shown in Eq. (5), the contact force $\boldsymbol{F}_C$ consists of normal and tangential components:

$$\boldsymbol{F}_c = \boldsymbol{F}_{c,n} + \boldsymbol{F}_{c,t} \tag{5}$$

The interaction between particles is modeled as a soft sphere contact process, and small overlaps are allowed to represent deformations, as shown in Fig. 1.

In Fig. 1, δ_n and δ_n are the displacements in the normal and tangential directions, respectively, due to particle collisions. The Hertz–Mindlin no-slip model simplifies the collision process using a spring and a damper. The damping coefficient is nonlinear (Tsuji et al., 1992), which helps simulate the actual energy dissipation. Figure 2 displays the constitutive model.

The $F_{c,n}$ calculation is based on Hertzian contact theory (Hertz, 1882), and the $F_{c,t}$ calculation is based on Mindlin-Deresiewicz's work (Mindlin, 1949; Mindlin & Deresiewicz, 1953).

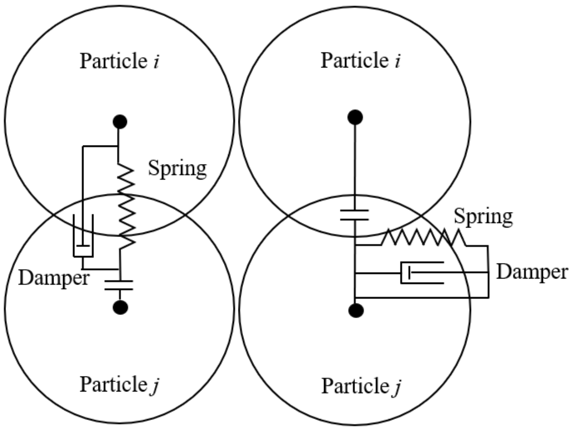

(a) Normal contact (b) Tangential contact
Fig. 2. Constitutive model of particle collision.

$$\boldsymbol{F}_{c,n} = -k_n\delta_n^{\frac{3}{2}}\boldsymbol{n} - \eta_n\boldsymbol{v}_n \tag{6}$$

$$\boldsymbol{F}_{c,t} = -\min\left(k_t\delta_t\boldsymbol{n} + \eta_t\boldsymbol{v}_t, \mu_s\left|\boldsymbol{F}_{c,n}\right|\right) \tag{7}$$

where k_n and k_t are the normal and tangential spring stiffness, respectively, η_n and η_t are the normal and tangential damping coefficients, respectively, and $\boldsymbol{v}_n$ and $\boldsymbol{v}_t$ are the normal and tangential relative velocities, respectively. These quantities are expressed as follows (Cundall & Strack, 1979; Tsuji et al., 1992):

$$k_n = E_{ij}\sqrt{R_{ij}} \tag{8}$$

$$E_{ij} = \left(\frac{1-v_i^2}{E_i} + \frac{1-v_j^2}{E_j}\right)^{-1}, \quad R_{ij} = R_iR_j/\left(R_i + R_j\right) \tag{9}$$

$$\eta_n = \sqrt{\frac{5}{4}k_n m_{ij}\delta_n^{\frac{1}{2}}} \cdot \frac{2\ln e}{\sqrt{\ln^2 e + \pi^2}}, \quad m_{ij} = m_i m_j/\left(m_i + m_j\right) \tag{10}$$

$$k_t = 8G_{ij}\sqrt{R_{ij}\delta_n}, \quad G_{ij} = \left(\frac{2-u_i}{G_i} + \frac{2-u_j}{G_j}\right)^{-1} \tag{11}$$

where E, v, R, e, and G are the Young's modulus, Poisson's ratio, radius, restitution coefficient, and shear modulus of the particles.

2.3 Fluid–Particle Coupling Model

2.3.1 Forces from the Fluid to the Particles

Drag force is dominant for particles in fluid flow. Thus, the selection of the drag model has a great effect on the particle motion, especially for cylindrical particles. Buettner et al. (2021) demonstrated the deficiencies of current spherical models when applied to non-spherical particles. In this paper, the drag models developed by Di Felice (1993), Haider and Levenspiel (1988), and Ganser (1993) are considered.

According to the model of Di Felice, the force on an isolated particle is calculated and altered by the influence of surrounding particles, and can be applied to non-spherical particles (Vollmari et al., 2016).

$$\boldsymbol{F}_d = \boldsymbol{F}_{d0}\alpha_f^{-(\gamma+1)} \tag{12}$$

$$\gamma = 3.7 - 0.65\exp\left[-\frac{\left(1.5-\log_{10} Re_p\right)^2}{2}\right] \tag{13}$$

where Re_p is the Reynolds number of the particles and $\boldsymbol{F}_{d0}$ represents the fluid drag force acting on a single particle, which is given by

$$\boldsymbol{F_{d0}} = \frac{1}{2}\rho_f C_D \frac{\pi d_p^2}{4}\alpha_f^2 \left|u - \boldsymbol{v_p}\right|\left(\boldsymbol{u} - \boldsymbol{v_p}\right) \tag{14}$$

where $\boldsymbol{v_p}$ is the particle velocity, and C_D is the drag coefficient:

$$\begin{cases} C_D = \dfrac{24}{Re_p} & Re_p \le 1 \\ C_D = \left(0.63 + \dfrac{4.8}{Re_p^{\ 0.5}}\right)^2 & Re_p > 1 \end{cases} \tag{15}$$

$$Re_p = \frac{\rho_f d_p \alpha_f \left|\boldsymbol{u} - \boldsymbol{v_p}\right|}{\mu_f} \tag{16}$$

For non-spherical particles, Haider and Levenspiel developed the drag model for a single non-spherical particle. The drag coefficient C_D was constructed according to experimental data points, and the particle shape factor φ was used to characterize irregular particles.

$$C_{D0} = \frac{24}{\mathrm{Re}_p}\left(1 + b_1 \mathrm{Re}_p^{\ b_2}\right) + \frac{b_3 \mathrm{Re}_p}{b_4 + \mathrm{Re}_p} \tag{17}$$

where

$$b_1 = \exp\left(2.3288 - 6.4581\varphi + 2.4486\varphi^2\right)$$
$$b_2 = 0.0964 + 0.5565\varphi$$
$$b_3 = \exp\left(4.905 - 13.8944\varphi + 18.4222\varphi^2 - 10.2599\varphi^3\right)$$
$$b_4 = \exp\left(1.4681 + 12.2584\varphi - 20.7322\varphi^2 + 15.8855\varphi^3\right)$$

The shape factor φ is defined as

$$\varphi = \frac{s}{S} \tag{18}$$

where s is the surface area of a sphere having the same volume as the particle and S is the actual surface area of the particle.

Ganser's drag law has the form

$$C_D = \frac{24}{Re_p K_1}\left(1 + 0.1118\left(Re_p K_1 K_2\right)^{0.6567}\right) + \frac{0.4305 K_2}{1 + \dfrac{3305}{Re_p K_1 K_2}} \tag{19}$$

with $K_1 = \dfrac{3}{1 + 2\varphi^{-0.5}}$ and $K_2 = 10^{1.8148(-\log\varphi)^{0.5743}}$

The Magnus force $\boldsymbol{F_{RL}}$ arises when particles rotate in a fluid. In this case, the rotational lift coefficient C_{RL} is used to scale the force.

$$\boldsymbol{F_{RL}} = \frac{1}{2}A_p C_{RL}\rho_f \frac{|\boldsymbol{v_p}|}{|\boldsymbol{\Omega}|}\left(\boldsymbol{v_p} \times \boldsymbol{\Omega}\right) \tag{20}$$

where A_p is the projected particle surface area and $\boldsymbol{\Omega}$ is the relative fluid–particle angular velocity. According to Rubinow and Keller (1961), C_{RL} is linearly proportional to the spin parameter S_{spin}:

$$C_{RL} = 2S_{spin} \tag{21}$$

The virtual mass and pressure gradient forces become significant and must be considered when the density ratio ($\dfrac{\rho_f}{\rho_p}$) is greater than 0.1. The virtual mass force required to accelerate the fluid surrounding the particle can be calculated as

$$\boldsymbol{F_{vm}} = C_{vm}\frac{\rho_f}{\rho_p}\left(\boldsymbol{v_p}\nabla\boldsymbol{u} - \frac{d\boldsymbol{v_p}}{dt}\right) \tag{22}$$

where C_{vm} is the virtual mass factor, which has a default value of 0.5.

The pressure gradient force can be written as

$$\boldsymbol{F_p} = \frac{\rho_f}{\rho_p}\boldsymbol{v_p}\nabla\boldsymbol{u} \tag{23}$$

2.3.2 Forces from Particles to the Fluid

Based on Newton's third law, the forces imposed by the particles on the fluids in a CFD cell can be calculated as

$$\boldsymbol{F}_s = \frac{-\sum_{i=1}^{n}\left(\boldsymbol{F}_d^i + \boldsymbol{F}_{RL}^i + \boldsymbol{F}_{vm}^i + \boldsymbol{F}_P^i\right)}{V_{cell}} \tag{24}$$

where V_{cell} is the volume of the cell and n represents the total number of particles in the cell.

2.4 Erosion Model

The Archard model is used to estimate the erosion depth on eroded surfaces. Archard (1953) investigated the contact mechanism and stated that the amount of material removed from the surface would be proportional to the frictional work done by particles moving over the surface:

$$Q = \frac{K d_t P}{H} \tag{25}$$

where Q represents the volume of removed material (mm^3). K is a dimensionless constant related to the material itself, and is taken as 3×10^{-3} m^2/N according to the experimental data of Chen *et al.* (2017). H is the hardness of the wall (HB), d_t is the tangential distance moved (mm), and P is the applied load (N).

2.5 Experimental Setup

To assess the accuracy of the various drag models, an experimental platform is designed and constructed for photographing the particle dispersion. Figure 3 shows the arrangement of the experiment. The two-phase mixture is stirred in the water tank, then pumped into the pipeline and

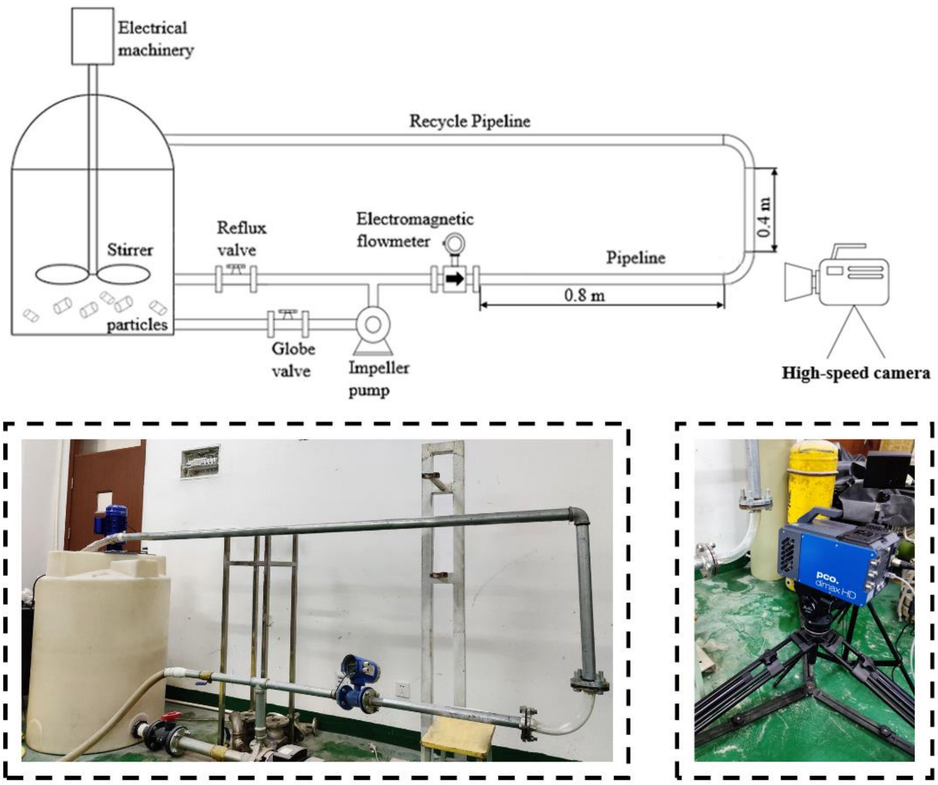

Fig. 3. Liquid-solid circulation experimental device.

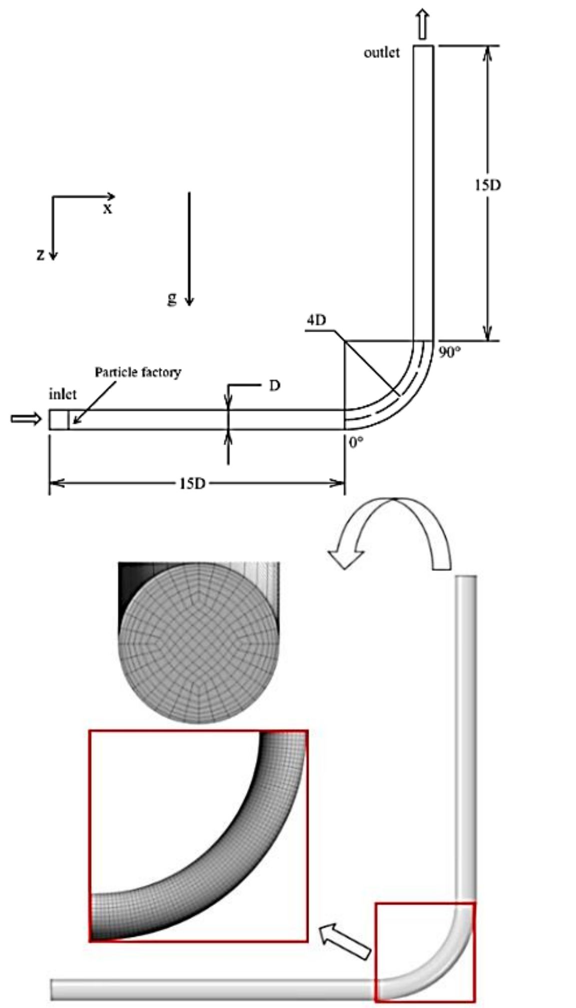

Fig. 4. Computational geometry and mesh used in the simulations.

flows through the reflux valve, the electromagnetic flowmeter, and the clear acrylic elbow. High-frequency porcelain cylindrical particles with a 1-mm bottom diameter and 2-mm height are used. The inner diameter D of the elbow is 34 mm and the radius of curvature R is 4D (=136 mm). The display resolution of the high-speed camera (model PCO.dimax HS4) is 1920×1080 pixels, which is sufficient so that the particles are visible when they pass through the transparent segment. The exposure time is set as 0.59 ms and the frame rate is 1547 fps.

2.6 Numerical Simulation Setup

The dimensions of the elbow simulation model are the same as in the experiment. To allow the flow to become fully developed, the lengths of both the horizontal and vertical straight pipes are 15D. As presented in Fig. 4, a three-dimensional hexahedral structured mesh is used to discretize the computational domain and ensure sufficient accuracy and stability. The maximum skewness value of the mesh is less than 0.6. Eight boundary layers are meshed in the near-wall region, with the first-layer height equal to 0.275 mm and a growth rate of 1.2. The value of y^+ is controlled in the range 30–300, which satisfies the requirements for the wall function. The coupling interface development is based on unresolved models, so the cell volume must be greater than the particle volume. Moreover, considering the stability of the solver and the accuracy of the drag model, the volume ratio is recommended to be greater than 10. Under these cell size requirements, mesh independence tests are conducted by examining the maximum erosion rate. Figure 5 shows the test result for four meshes. As the mesh is gradually refined, the erosion rate tends to stabilize. In view of improving computing efficiency, the number of mesh cells is determined as 15×10^4 for the numerical simulations.

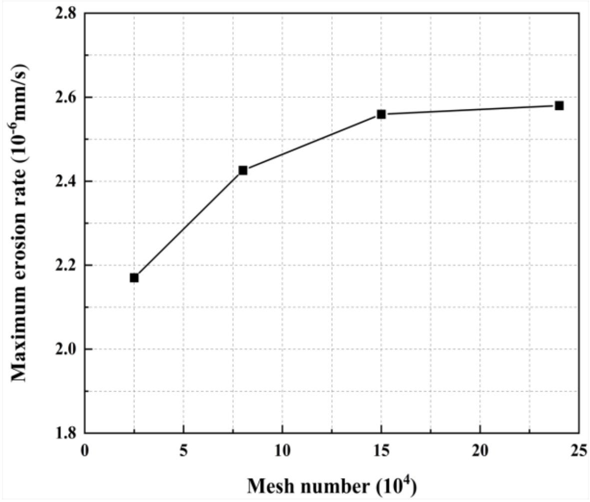

Fig. 5. Mesh independency study.

Table 1 Catalyst particles with different aspect ratios (Ar).

	Ar=1	Ar=2	Ar=3	Ar=4
DEM model				
Spheres	1	143	207	296

Non-spherical particles are constructed with the multi-sphere clump method. A grid is generated around the cylinder to ensure the fidelity of the multi-sphere particles.

The cylindrical particles are combined with spheres of different sizes, as described in Table 1. The Monto Carlo method is adopted to calculate the centroid, mass, and inertial tensors of the non-spherical particles.

In the CFD calculations, a pressure-based solver is used. The fluid phase is water. The inlet is set as a velocity inlet, the outlet is set as a pressure outlet (0 Pa), and the remaining boundaries are no-slip walls. To discretize the pressure, momentum, turbulent kinetic energy, and specific dissipation rate calculations, a second-order upwind scheme is adopted. The SIMPLEC method is applied to ensure pressure–velocity coupling. The time step size is set as 1×10^{-4} s. The DEM settings are listed in Table 2. For particle–particle interactions, the coefficients of restitution, static friction, and rolling friction are 0.5, 0.6, and 0.05, respectively. For particle–wall interactions, the corresponding coefficients are 0.5, 0.4, and 0.05.

3. Results and Discussion

3.1 Effect of Drag Models on Particle Motion

By adjusting the valve openings, flow velocities of 2 m/s, 3 m/s, and 4 m/s were achieved. After the flow had become stable, the spatial distribution of the particles was as shown in Fig. 6. The number of particles varies slightly at different speeds due to the different carrying capacities. The calculation results using the different drag models are also shown.

Table 2 Calculation parameters of DEM

Item	Details	Value
Particle	Poisson’s ratio	0.25
	Shear modulus(Pa)	1×10^{8}
	Density(kg·m^{-3})	3000
Wall	Poisson’s ratio	0.32
	Shear modulus(Pa)	2.5×10^{10}
	Density(kg·m^{-3})	7800
Time step	Fixed time step(s)	1×10^{-6}

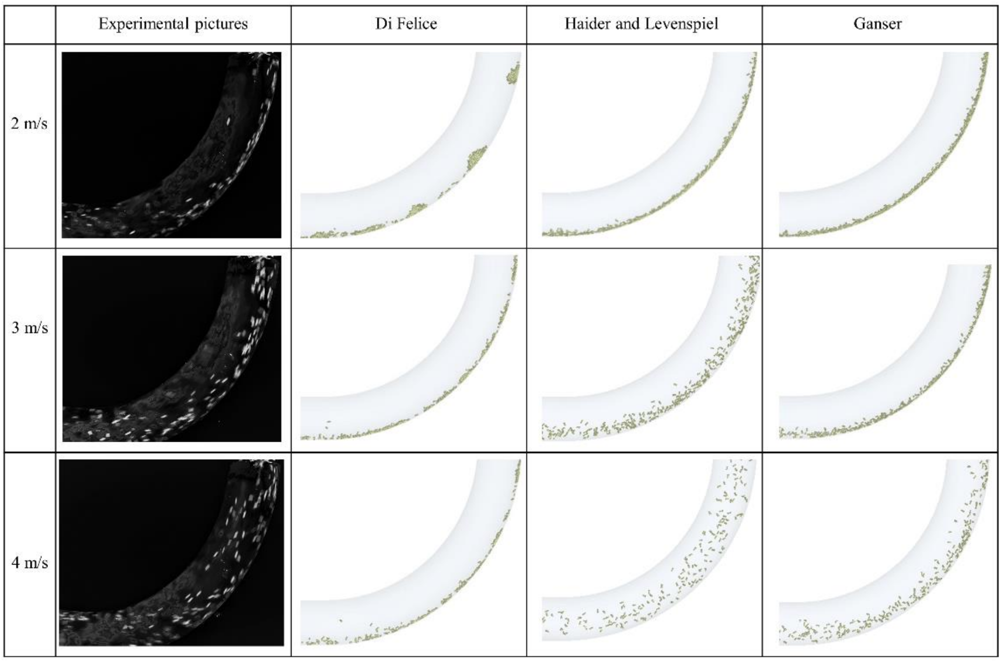

Fig. 6. Comparison of particle spatial distribution in simulations and experiments.

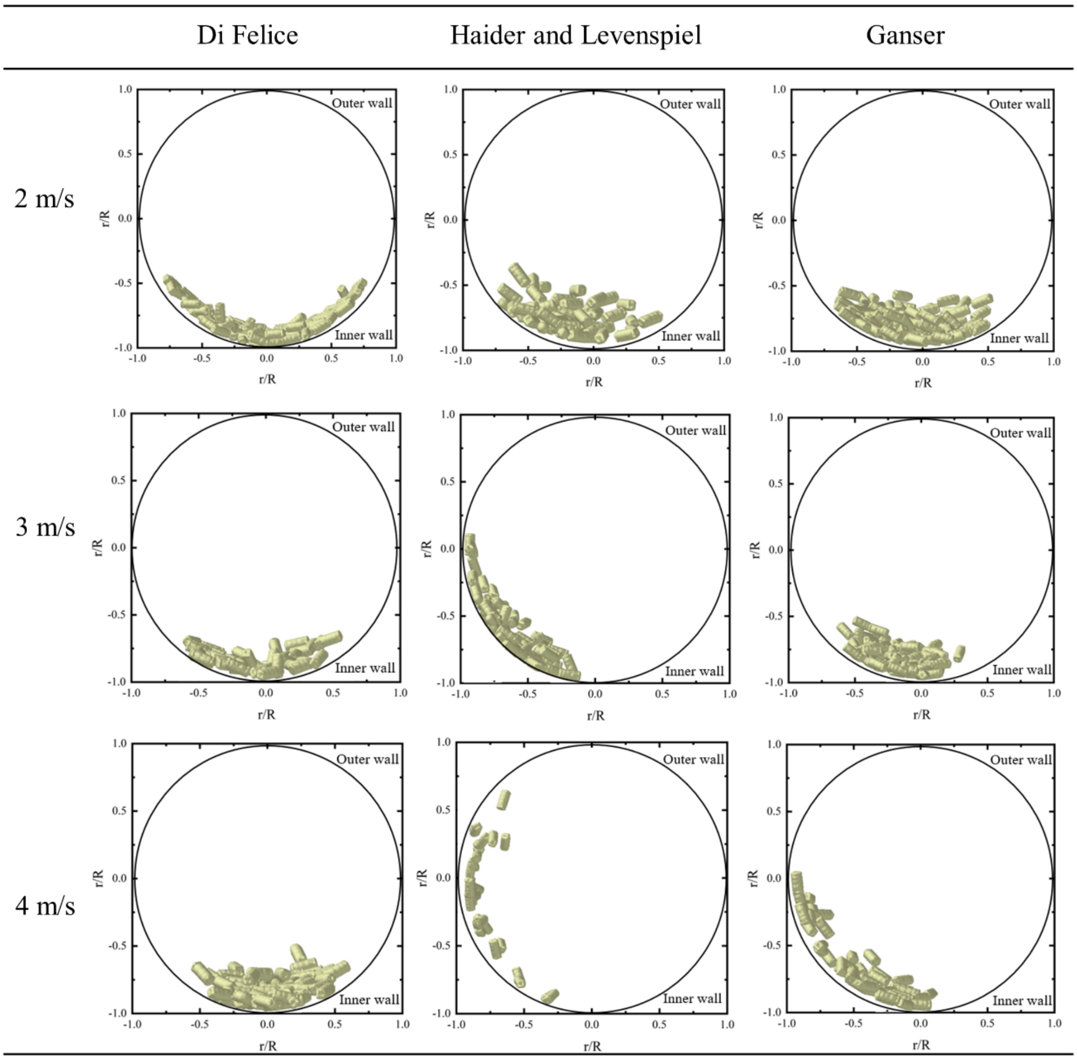

Fig. 7. Poincare map of particles with different drag models.

Figure 6 indicates that when the flow velocity is 2 m/s, the particles are affected by the drag force, which restricts the particle movement within streamlines. In parallel, gravity causes the particles to settle, effectively restricting their motion to the bottom of the pipe wall. Particle–particle and particle–wall interactions are weak. The particles are close to the outer wall and slide when entering the bend section. In a given region, the particles have approximately the same movement direction. With an increase in velocity, the distribution of the particles becomes more dispersed and gradually covers the entire flow field. The trend is more visible at 4 m/s. The particles have a broader range of motion at axial angles of 54°–72°. This implies that the region of most severe erosion will shift towards the elbow inner wall at higher flow velocities.

The drag force directly influenced the particle motion. Numerical simulations using the Di Felice drag model show an obvious aggregation phenomenon at the outer walls at 2 m/s. There is almost no difference in the spatial distributions of the particles as the speed increases. Poincare maps are used to display the particle motion at a cross-section in Fig. 7. The Haider & Levenspiel drag model and the Ganser drag model both reflect the particle trend of moving the inner wall, while the Di Felice drag model does not. Stokes number can explain such a trend and will be present in the following section. Figure 8 shows that these particles have high average velocities in the z-direction (i.e., along the negative Z-axis). The spatial distribution of particles is more dispersed and closer to the experimental situation when using the Haider &

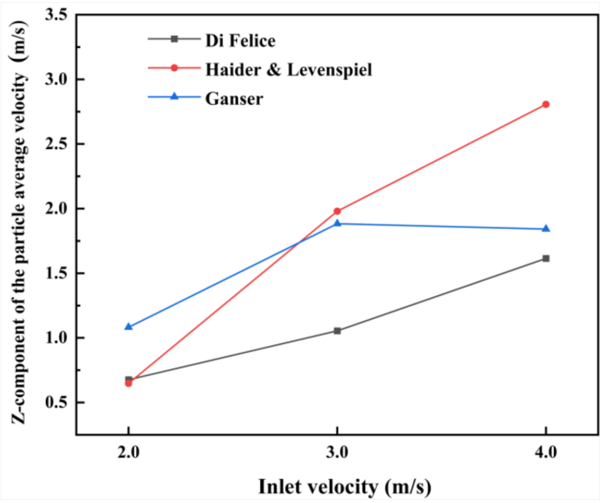

Fig. 8. Influence of drag models on particle average velocities in z-direction.

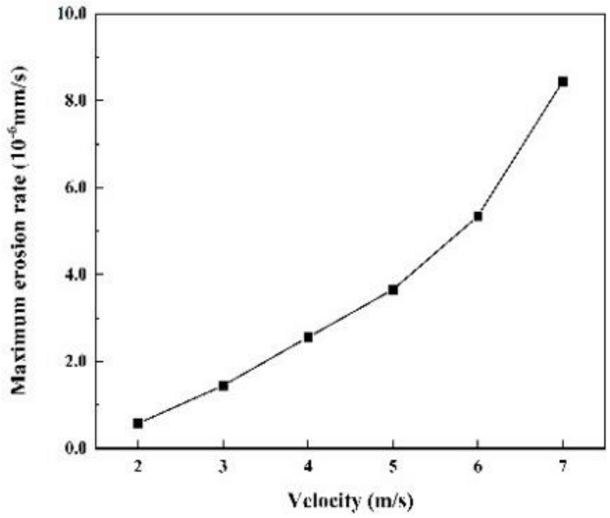

Fig. 9. Influence of inlet velocity on maximum erosion rate.

Levenspiel drag model under flow velocities of 3 m/s and 4 m/s. The z-component of velocity with the Haider & Levenspiel drag model increases as the inlet velocity increases, whereas Ganser's drag model produces a slight decrease in the z-component of velocity at 4 m/s. In addition, Fig. 7 also presents the particle offset situation at 3 m/s and 4 m/s. It is associated with the secondary flow, and particles are driven from the compression side to the suction side.

Haider & Levenspiel, and Ganser models both consider the shape factor in the C_D calculation, and the simulated particle distribution based on a single non-spherical particle followed the trends of the experimental images. C_D for "the Haider Levenspiel drag model" is more applicable to cylindrical particles in liquid flow, and simulation based on the model can reflect the trend of particles shifting towards the inner wall with increasing inlet velocity, especially at 3 and 4 m/s.

3.2 Effect of Inlet Velocity on Erosion

As a higher inlet velocity results in greater impact energies, there is also a nearly exponential rise in the maximum erosion rate, as shown in Fig. 9. Clearly, the inlet velocity has a significant effect on erosion. According to the results displayed in Fig. 10(a), the maximum erosion rate changes slightly at different bend curvature angles for 2–5 m/s. When the flow velocities are 6 m/s and 7 m/s, the local maximum erosion rate occurs at 6°, 40°, and 73°. To provide a clearer view of these results, the maximum erosion rates along the inner and outer walls are plotted in Figs. 10(b) and 10(c), respectively. Increasing the inlet velocity alters the spatial distribution of particles, which contributes to friction between the particles and the inner walls. The position of maximum erosion shifts from the outer walls to the inner walls at 6 m/s. The maximum erosion rate along the inner wall is very similar at velocities of 5 m/s, 6 m/s, and 7 m/s. For the outer wall, the peak values are centered around 70°.

Figure 11 illustrates the particle trajectories and contours of erosion rate. For inlet velocities of 2 m/s and 3 m/s, the particles are limited to the bottom of the elbow due to the drag force and gravity. Hence, the particles only contact outer wall when passing through the bend section. According to Fig. 10(c), particles start to contact and separate from the walls at about 8° and 70°, and the main features are uniform shallow erosion in the middle and more serious damage at both ends. When the inlet velocity is from 4–7 m/s, the surface morphology of the outer wall shares similar characteristics and agrees with the particle trajectories. The trajectories can be generally divided into two parts: one set along the inner wall and another set

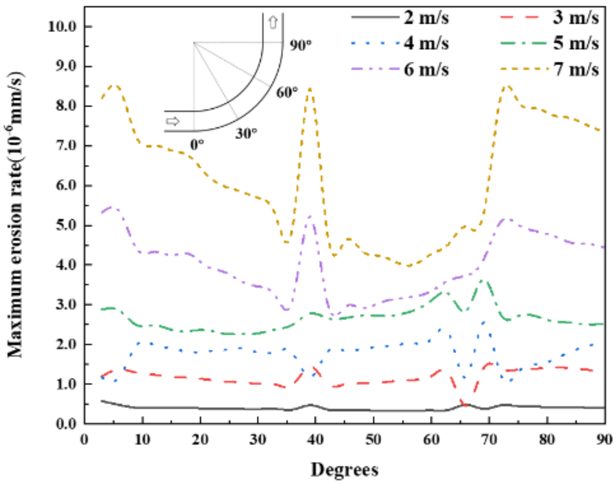

(a) Erosion rate around the whole elbow

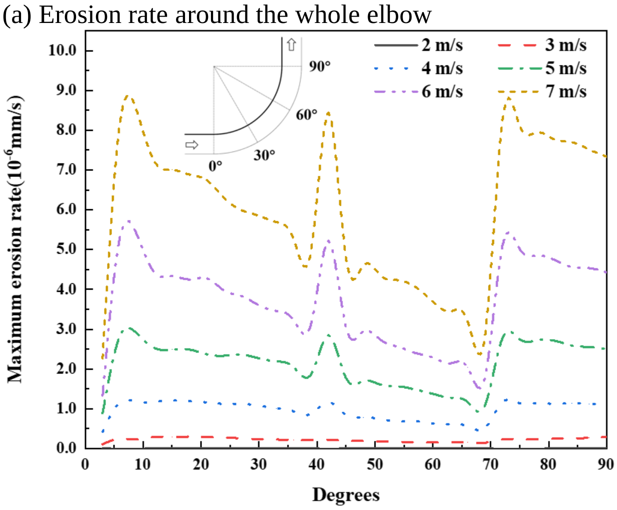

(b) Erosion rate along inner walls

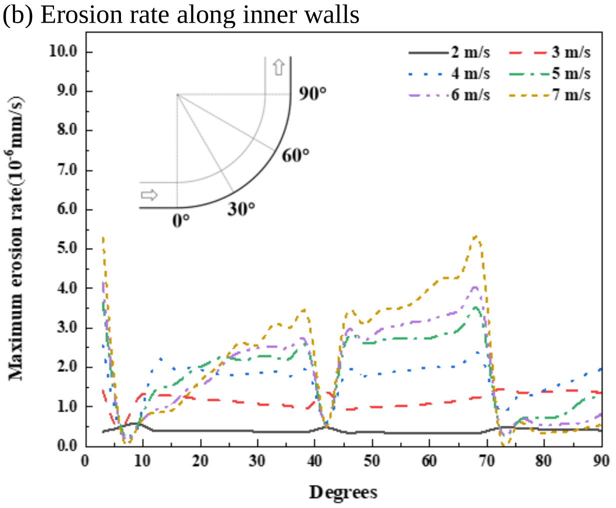

(c) Erosion rate along outer walls

Fig. 10. Influence of inlet velocity on maximum erosion rate along bend curvature angle.

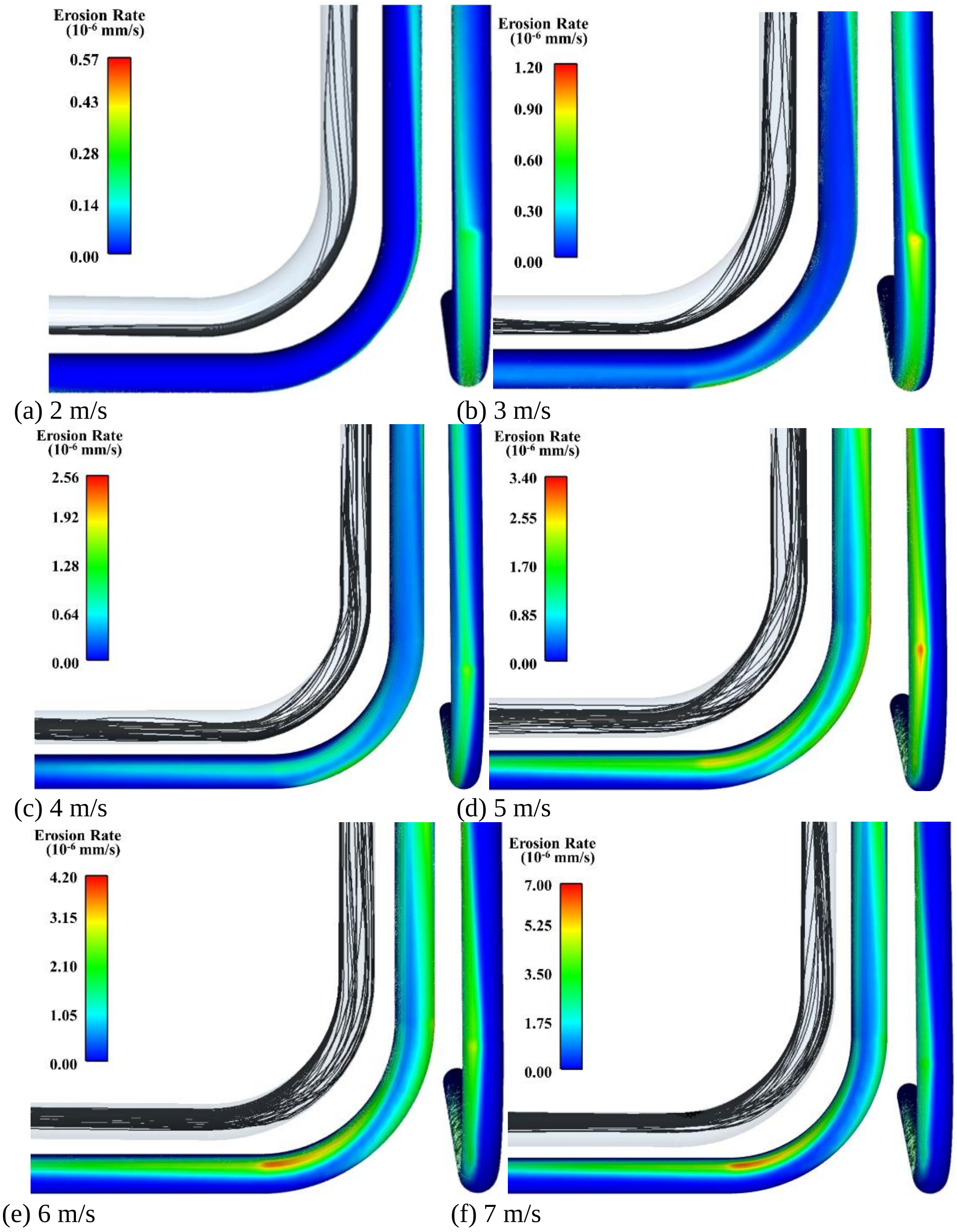

Fig. 11. Erosion profiles and particle trajectories of the elbow with different inlet velocities.

along the outer wall. Severe erosion areas along the inner wall are concentrated around the elbow's center and the extent of the particle distribution significantly increases in the section above the bending axis. Most particle trajectories turn towards the inner wall, which results in a change of the maximum erosion rate position at 6 m/s and 7 m/s. In the following, the Stokes number (*St*) is used to describe the erosion law with changes in inlet velocity.

Particles flowing through the elbow are mainly subjected to the particle inertial force and the drag force exerted by the fluid, which ensures the particles move along the tangential direction and prompts them to follow the water streamlines, respectively. The particle Stokes number is a measure of the ratio between the inertial force and drag force. This dimensionless number is related to the particle trajectories and is written as $\mathrm{St}=\frac{\rho_p d_p^2 u}{18(\mu D)}$. To analyze the erosion location, a dimensionless number λ is defined as the ratio of the inner wall's maximum erosion rate to that of the whole elbow. Figure 12 shows that λ increases as the Stokes number rises. For $St \geq 113.7$, λ stabilizes at a value of 1 and no longer changes. Furthermore, the inertial force plays a leading role and particles contain sufficient momentum to cross the vortex with a large Stokes number. In this case, particles deviate from the streamlines of the surrounding fluid and directly contact the inner wall. When $St \geq 113.7$, the maximum erosion rate occurs at the inner wall; when $St < 113.7$, it will occur at the outer wall.

The erosion traces move closer to the sidewalls with increases in velocity, which illustrates that cylindrical particles are susceptible to secondary flows. The secondary flow vortices are generated by the centrifugal effect and push the flow to the sidewalls. The velocity vectors at the plane perpendicular to the bend curvature angle of 90° are displayed in Fig. 13. A portion of the flow separates from the bulk flow, and one pair of counter-rotating vortices forms. Their intensity becomes stronger as the inlet velocity increases.

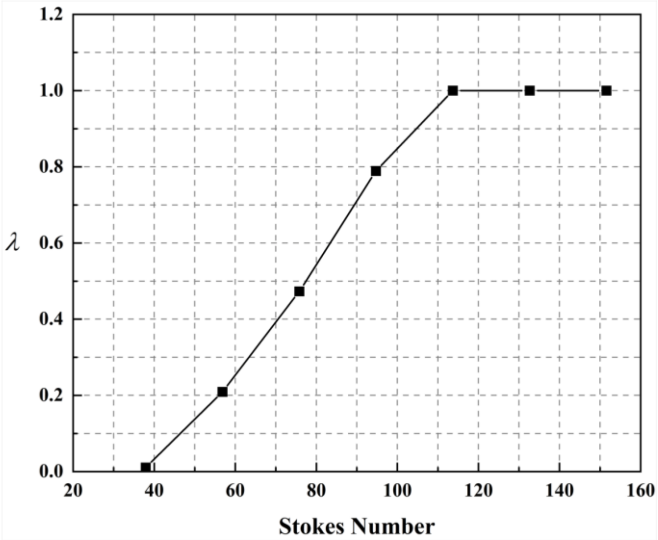

Fig. 12. Relationship between λ and *St*.

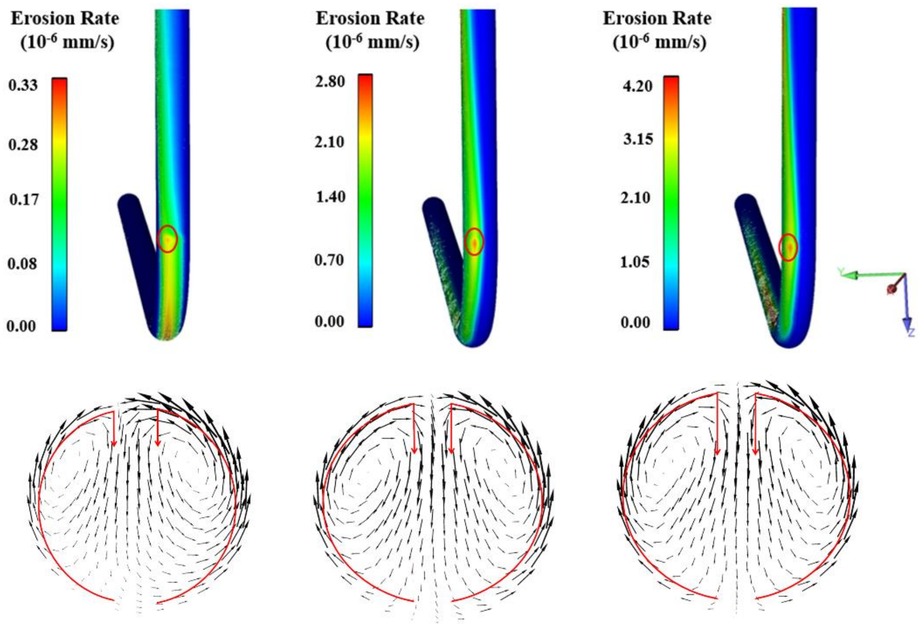

(a) 2 m/s (b) 5 m/s (c) 7 m/s

Fig. 13. Velocity vectors on a cross-section and erosion profiles of outer walls.

3.3 Effect of Particle Shape on Erosion

With the particle generation rate and the inlet velocity held constant at 0.2 kg/s and 4 m/s, numerical simulations were carried out with particle aspect ratios of 1, 2, 3, and 4. The maximum erosion rate decreases as the aspect ratio increases, as displayed in Fig. 14. This is because a higher aspect ratio means there are fewer particles, which reduces the impact density. Compared with spherical particles, cylindrical particles are subjected to a greater drag force. Table 3 presents the number of particle–wall collisions. Given the larger contact area, particles with *Ar*=2 and *Ar*=3 produce a greater number of collisions than spherical particles. The collision number is associated with the length of the sliding path.

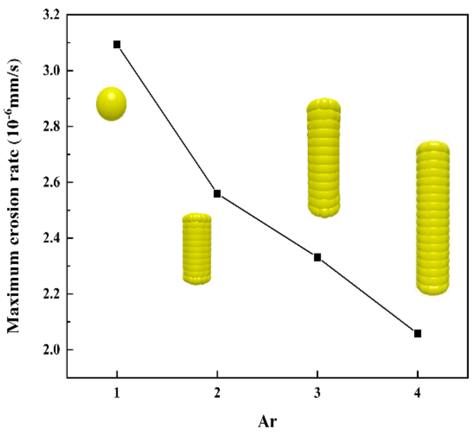

Fig. 14. Influence of aspect ratio *Ar* on maximum erosion rate.

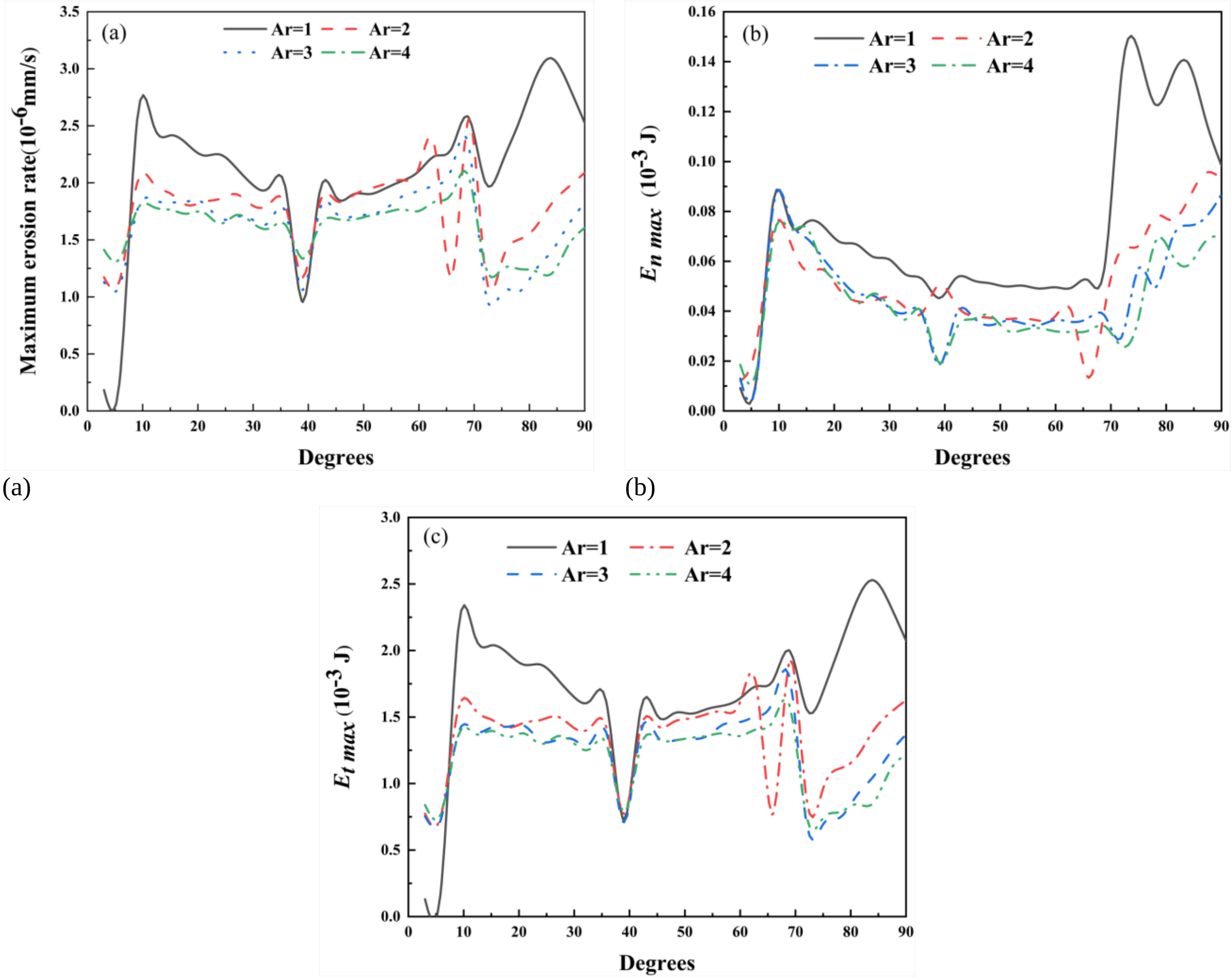

Fig. 15. Variation of (a) maximum erosion rate, (b) maximum normal cumulative contact energy, (c) maximum tangential cumulative contact energy along bend curvature angles.

Table 3 Statistical information of particles passing through the elbow

	Ar=1	*Ar*=2	*Ar*=3	*Ar*=4
Number of particles	52514	15057	11323	8799
Number of collisions (particle-particle)	10526	5051	3327	2563
Number of 1 (particle-wall)	8363	10443	9857	8263
Drag force (10^{-3} N)	0.25	1.06	1.48	1.85

To quantify the two modes of erosion on the elbow wall, the normal and tangential cumulative contact energies are introduced to measure the cumulative energy produced by material impacting and sliding, respectively. E_n and E_t are expressed as

$$E_n = \sum |F_n V_n \delta t| \tag{26}$$

$$E_t = \sum |F_t V_t \delta t| \tag{27}$$

where V_n is the normal relative velocity, which is negative in a loading situation, and V_t is the tangential relative velocity.

Figure.15 (b) illustrates impacting mode occurs mainly in the entrance and exit section of the elbow. Specifically, the maximum normal energy of the wall begins to increase at 5° and reaches a peak value at 10°. The curve exhibits a decreasing trend within the range of 10°–70°. This tendency is even more pronounced for cylindrical particles. At locations beyond 70°, where the downstream region is adjacent to the outlet, the maximum normal energy of cylindrical particles gradually increases. Spherical particles exhibit rapid growth in this region, with two maximum values. The maximum tangential energy curves display similar fluctuations, with a clear trough appearing at 40° and two peaks at 10° and 70°. Likewise, Fig.15(a) shows the sudden drop in erosion rate at 40° and 70°. This is because of the continuous particle-wall sliding and friction leading to reduce particle velocity. At this time, the particles will follow the fluid flow and separate from the wall at 40° and 70°. It is clear from Fig. 15(c) that spherical particles have a larger range of fluctuations.

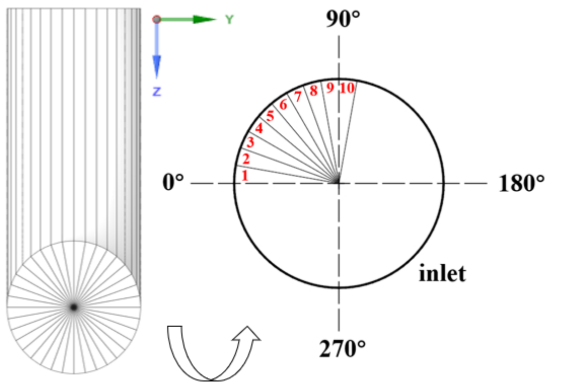

Fig. 16. Division of circumferential regions.

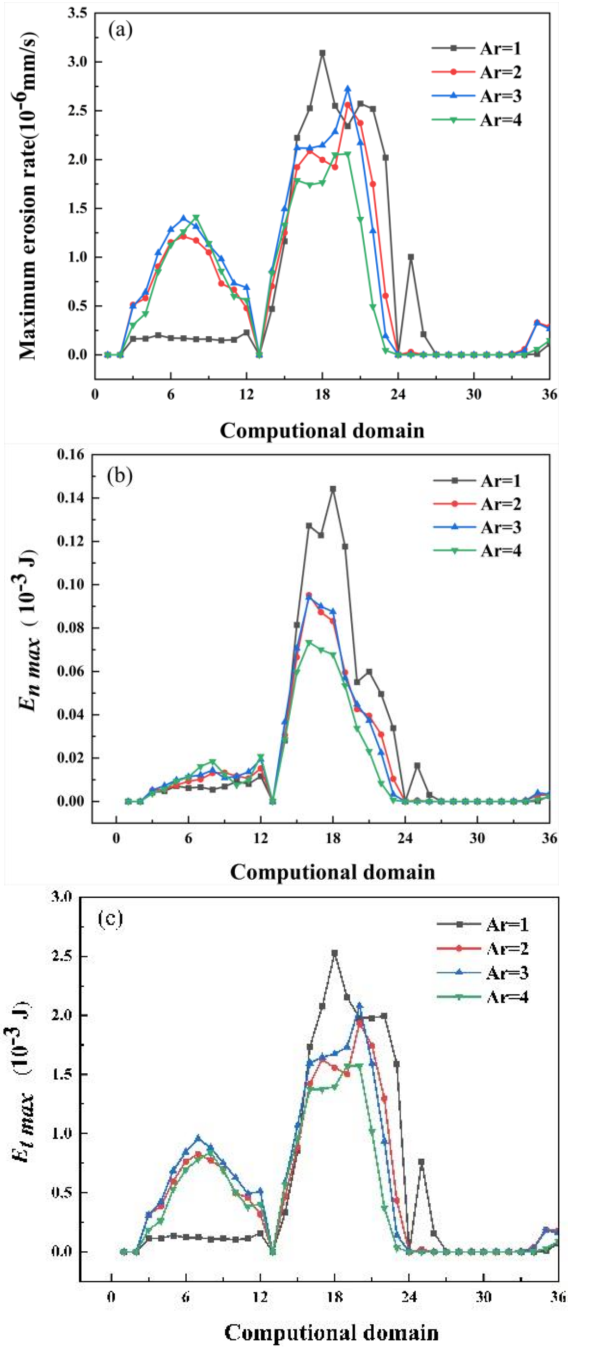

Fig. 17. Variation of (a) maximum erosion rate, (b) maximum normal cumulative contact energy, (c) maximum tangential cumulative contact energy along circumferential regions.

We now divide the circumferential erosion regions at 10° intervals, as shown in Fig. 16, so that computational domain 1 corresponds to circumferential angles of 0°–10°, and so on. Figure 17 shows the erosion and cumulative energy variation at different circumferential angles. The locations of severe erosion are distributed in the range of 170°–200° and the maximum erosion rate, which has a parabola-like profile, occurs from 120°–240°. There is a clear distinction in the erosion distribution between the spherical particles and the cylindrical particles. Spherical particles are almost unaffected by secondary flow and barely enter the area of 0°–120°, whereas cylindrical particles slide along the walls so that the wall normal energy is almost zero in this range (see Figs. 17(b) and 17(c)).

Spherical (Ar=1) and cylindrical particles (Ar=2, 3, and 4) exhibit distinct contact energy distributions. In either axial or circumferential direction, the contact energy distributions of cylindrical particles with Ar=2, 3, and 4 follow a similar trend. Overall, in the process of contacting the elbow walls, E_t is greater than E_n and can be written as $E_{t\ \max} = nE_{n\ \max}$. For particle aspect ratios of 1, 2, 3, and 4, n is equal to 17.6, 20.3, 20.5, and 21.5, respectively. And the curve representing tangential energy basically coincides with that of the erosion rate. On the other hand, the particle-wall collisions are high, and elbow erosion marks appear as stripes. All of this suggests that sliding is the predominant behavior during contact with the elbow walls.

4. CONCLUSION

A CFD-DEM coupling method has been used to calculate the elbow erosion rate produced by cylindrical particles composed of multi-sphere clumps. The effectiveness of various drag models was verified through comparisons against experimental results. Numerical simulations were performed under various inlet velocities and aspect ratio conditions. Based on the results, the following conclusions can be stated.

(1) The calculated particle distribution based on single non-spherical particle drag models followed the experimental images' trends. Using Haider Levenspiel model is more accurate to recreate cylindrical particles flow in an elbow, while simulation with the Di Felice drag model does not.

(2) A higher inlet velocity not only increases the kinetic energy of the particles, but also affects their spatial distribution, as indicated by the particle trajectories. Numerical simulation results show that the elbow erosion morphology is aligned with the particle trajectories. Most particle trajectories turn towards the inner wall, which results in the same position of maximum erosion at 6 m/s and 7 m/s. The critical Stokes number is identified as 113.7. Cylindrical particles are susceptible to secondary flows, which lead to a sidewall shift in the erosion traces.

(3) Given the same particle quality, the impact density decreases with increasing aspect ratio, resulting in a reduction in the maximum erosion rate. According to the collision number statistics, sliding is the predominant

contact mode. Furthermore, E_n and E_t were introduced to quantify the impacting and sliding, respectively. E_n is greater than E_t and can be written as $E_{t\max} = nE_{n\max}$. For particle aspect ratios of 1, 2, 3, and 4, n is equal to 17.6, 20.3, 20.5, and 21.5, respectively.

ACKNOWLEDGEMENTS

The authors are grateful to the National Natural Science Foundation of China (Grant Nos. 52176048, 51876194, U1909216).

CONFLICT OF INTEREST

The authors declare that they have no known competing financial interests or personal relationships that could have appeared to influence the work reported in this paper.

AUTHORS CONTRIBUTION

Haozhe Jin: Project administration, Resources, Funding acquisition. Zeyu Liao: Writing-original draft, Writing-review & editing, Visualization, Investigation. Junfeng Zhou: Data curation, Investigation. Xiaofei Liu: Supervision, Writing-review & editing. Hongchi Yao: Investigation. Chao Wang: Supervision, Writing-review & editing.

REFERENCES

Adedeji, O. E., & Duarte, C. R. (2020). Prediction of thickness loss in a standard 90° elbow using erosion-coupled dynamic mesh. *Wear*, 460-461(2020), 203400. https://doi.org/10.1016/j.wear.2020.203400

Ahlert, K. (1994). *Effect of particle impingement angle and surface wetting on solid particle erosion of aisi 1018 steel* [MS Thesis]. University of Tulsa, Oklahoma, United States.

Ali, H. M. (2022). Phase change materials based thermal energy storage for solar energy systems. *Journal of Building Engineering*, 56(2022), 104731. https://doi.org/10.1016/j.jobe.2022.104731

Archard, J. F. (1953). Contact and rubbing of flat surfaces. *Journal of Applied Physics*, 24(8), 981-988. https://doi.org/10.1063/1.1721448

Bitter, J. G. A. (1962). A study of erosion phenomena. *Wear*, 6, 5-21. https://doi.org/10.1016/0043-1648(63)90003-6

Buettner, K. E., Curtis, J. S., & Sarkar, A. (2021). Fluid–particle drag force measurements from particle-resolved CFD simulations of flow past random arrays of ellipsoidal particles. *Chemical Engineering Science*, 235, 116469. https://doi.org/10.1016/j.ces.2021.116469

Chen, G., Liu, Y., & Lodewijks, G. (2017). Experimental research on the determination of the coefficient of sliding wear under iron ore handling conditions. *Tribology in Industry*, 39(3), 378-390. https://doi.org/10.24874/ti.2017.39.03.13

Chen, J., Wang, Y., & Li, X. (2015). Erosion prediction of liquid–particle two-phase flow in pipeline elbows via CFD–DEM coupling method. *Powder Technology*, 275, 182-187. https://doi.org/10.1016/j.powtec.2014.12.057

Chen, L., Sun, Z., & Ma, H. (2022). Energy loss caused by the elbow of stiff shotcrete pneumatic conveying based on response surface method and CFD-DEM. *Powder Technology*, 408, 117726. https://doi.org/10.1016/j.powtec.2022.117726

Cundall, P. A., & Strack, O. D. L. (1979). A discrete numerical model for granular assemblies. *Géotechnique*, 29(1), 47-65. https://doi.org/10.1680/GEOT.1979.29.1.47

Deng, T., Bingley, M. S., & Bradley, M. S. A. (2004). The influence of particle rotation on the solid particle erosion rate of metals. *Wear*, 256(11-12), 1037-1049. https://doi.org/10.1016/S0043-1648(03)00536-2

Di Felice, R. (1993). The voidage function for fluid-particle interaction systems. *International Journal of Multiphase Flow*, 20, 153-159. https://doi.org/10.1016/0301-9322(94)90011-6

Finnie, I. (1960). Erosion of surfaces by solid particles. *Wear*, 3, 87-103. https://doi.org/10.1016/0043-1648(60)90055-7

Finnie, I., & McFadden, D. H. (1979). On the velocity dependence of the erosion of ductile metals by solid particles at low angles of incidence. *Wear*, 48, 181-190. https://doi.org/10.1520/STP35794S

Ganser, G. H. (1993). A rational approach to drag prediction of spherical and nonspherical particles. *Powder Technology*, 77, 143-152. https://doi.org/10.1016/0032-5910(93)80051-B

Gao, S. Q., Jin, H. Z., & Ou, G. F. (2022). Erosion behaviors of gas–solid flow on an assignment plate using CFD–DEM. *Journal of Applied Fluid Mechanics*, 15(5), 1609-1620. https://doi.org/10.47176/JAFM.15.05.33598

Haider, A., & Levenspiel, O. (1989). Drag coefficient and terminal velocity of spherical and nonspherical particles. *Powder Technology*, 58, 63-70. https://doi.org/10.1016/0032-5910(89)80008-7

Hertz, H. (1882). On the contact of elastic solids. *Journal fur die Reine und Angewandte Mathematik*, 1882(92), 156-171.

Jing, J., Xiao, F., & Yang, L. (2018). Measurements of velocity field and diameter distribution of particles in multiphase flow based on trajectory imaging. *Flow Measurement and Instrumentation*, 59, 103-113. https://doi.org/10.1016/j.flowmeasinst.2017.12.005

Liu, X. F., Zhou, J. F., & Gao, S. Q. (2022). Study on the impact wear characteristics of catalyst particles at 90° elbow via CFD-DEM coupling method. *Journal of Applied Fluid Mechanics*, 15(1), 221-230. https://doi.org/10.47176/JAFM.15.01.32536

Lu, G., Third, J. R., & Muller, C. R. (2012). Critical assessment of two approaches for evaluating contacts between super-quadric shaped particles in DEM simulations. *Chemical Engineering Science*, 78, 226-235. https://doi.org/10.1016/j.ces.2012.05.041

Mindlin, R. D., & Deresiewicz, H. (1953). Elastic Spheres in Contact under Varying Oblique Force. *Journal of Applied Mechanics,* 20(1), 327-344. https://doi.org/10.1007/978-1-4613-8865-4_35

Mindlin, R. D. (1949) Compliance of elastic bodies in contact. *Journal of Applied Mechanics*, 16 259-268. https://doi.org/10.1007/978-1-4613-8865-4_24

Oka, Y. I., & Yoshida, T. (2005). Practical estimation of erosion damage caused by solid particle impact. *Wear,* 259(1-6), 95-109. https://doi.org/10.1016/j.wear.2005.01.039

Ou, G., Cao, X., & Wang, C. (2022). CFD-DEM-based numerical simulation of erosion characteristic of multistage pressure relief string regulating valve. *Journal of Applied Fluid Mechanics,* 15(4), 999-1015. https://doi.org/10.47176/JAFM.15.04.1022

Rubinow, S. I., & Keller, J. B. (1961). The transverse force on a spinning sphere moving in a viscous fluid. *Journal of Fluid Mechanics*, 11(03), 447. https://doi.org/10.1017/S0022112061000640

Sajjad, U., Hussain, I., & Hamid, K. (2022). Liquid-to-vapor phase change heat transfer evaluation and parameter sensitivity analysis of nanoporous surface coatings. *International Journal of Heat and Mass Transfer*, 194(2022), 123088. https://doi.org/10.1016/j.ijheatmasstransfer.2022.123088

Singh, V., Kumar, S., & Mohapatra, S. K. (2019). Modeling of erosion wear of sand water slurry flow through pipe bend using CFD. *Journal of Applied Fluid Mechanics,* 12(3), 679-687. https://doi.org/10.29252/jafm.12.03.29199

Tsuji, T., Yabumoto, K., & Tanaka, T. (2008). Spontaneous structures in three-dimensional bubbling gas-fluidized bed by parallel DEM–CFD coupling simulation. *Powder Technology,* 184(2), 132-140. https://doi.org/10.1016/j.powtec.2007.11.042

Tsuji, Y., Tanaka, T., & Ishida, T. (1992). Lagrangian numerical simulation of plug flow of cohesionless particles in a horizontal pipe. *Powder Technology,* 71(3), 239-250. 10.1016/0032-5910(92)88030-L

Vollmari, K., Jasevičius, R., & Kruggel-Emden, H. (2016). Experimental and numerical study of fluidization and pressure drop of spherical and non-spherical particles in a model scale fluidized bed. *Powder Technology*, 291, 506-521. https://doi.org/10.1016/j.powtec.2015.11.045

Wang, J., Zhang, M., & Feng, L. (2020). The behaviors of particle-wall collision for non-spherical particles: Experimental investigation. *Powder Technology,* 363, 187-194. https://doi.org/10.1016/j.powtec.2015.11.045

Wang, K., Li, X., & Wang, Y. (2017). Numerical investigation of the erosion behavior in elbows of petroleum pipelines. *Powder Technology,* 314, 490-499. https://doi.org/10.1016/j.powtec.2016.12.083

Wang, Q., Huang, Q., & Wang, N. (2021). An experimental and numerical study of slurry erosion behavior in a horizontal elbow and elbows in series. *Engineering Failure Analysis,* 130, 105779. https://doi.org/10.1016/j.engfailanal.2021.105779

Yu, A. B. & Xu, B. H. (2003). Particle-scale modelling of gas-solid flow in fluidization. *Journal of Chemical Technology & Biotechnology,* 78(2-3), 111-121. https://doi.org/10.1002/jctb.788

Zeng, D. Z., Zhang, E. B., & Ding, Y. Y. (2018). Investigation of erosion behaviors of sulfur-particle-laden gas flow in an elbow via a CFD-DEM coupling method. *Powder Technology*, 329, 115-128. https://doi.org/10.1016/j.powtec.2018.01.056

Zhou, J. W., Liu, Y., & Liu, S. Y. (2017). Effects of particle shape and swirling intensity on elbow erosion in dilute-phase pneumatic conveying. *Wear,* 380-381, 66-67. https://doi.org/10.1016/j.wear.2017.03.009

Zolfagharnasab, M. H., Salimi, M., & Zolfagharnasab, H. (2021). A novel numerical investigation of erosion wear over various 90-degree elbow duct sections. *Powder Technology,* 380, 1-17. https://doi.org/10.1016/j.powtec.2020.11.059